



# Performance improvement of existing drag models in two-fluid modeling of gas–solid flows using a PR-DNS based drag model

Ahmadreza Abbasi Baharanchi<sup>a,b</sup>, Seckin Gokaltun<sup>a,\*</sup>, George Dulikravich<sup>b</sup>

<sup>a</sup> Applied Research Center, Florida International University, 10555 W Flagler St., EC2100, Miami, FL 33174, United States

<sup>b</sup> Department of Mechanical and Materials Engineering, Florida International University, 10555 W Flagler St., EC3462, Miami, FL 33174, United States

## ARTICLE INFO

### Article history:

Received 17 December 2014

Received in revised form 12 May 2015

Accepted 3 July 2015

Available online 16 July 2015

### Keywords:

Multiphase flow

CFD

MFIX

Drag model

Two-fluid

Fluidized bed

## ABSTRACT

This paper investigates a new drag model for the simulation of the fluidization of fluid catalytic cracking (FCC) particles with air in a fluidized bed using the two-fluid model (TFM) within the Multiphase Flow with Interphase Exchanges (MFIX) code. A cohesion index parameter based on the interparticle cohesive forces has been implemented in the MFIX-TFM code. This index is used as a switching criterion between a particle resolved drag model developed by Tenneti et al. (2011), and some of the drag models available in the MFIX for homogeneous particles, namely the Gidaspow, Syam–O'Brien, and Wen–Yu models. The proposed drag correlation in this paper implements an indirect method of introducing interparticle cohesive forces to our TFM simulations. Significant improvement in the solid volume fraction profile along the riser was obtained for all of the drag law combinations, depending on the conditions set in the switching procedures. In the best case, the utilization of the Gidaspow and TGS models resulted in a 60% improvement in maximum deviation of numerical results from the available experimental data. The proposed model can be used in simulations of fluidized beds, where standard models fail to produce accurate results even on extremely refined computational grid, especially for Geldart A type particles that may exhibit strong clustering behavior.

© 2015 Elsevier B.V. All rights reserved.

## 1. Introduction

The TFM approach, developed by van Deemter and van der Laan [42], is known as an economic way of simulating multiphase flows in large-scale fluidized bed risers [30]. Formulating the solid and gas as continuous phases is the principle of the TFM method. This leads to significant reduction of memory and computational costs as compared to other widely exploited methods, such as the Particle-Resolved Direct Numerical Simulation [16,29], Discrete Element Method [27,41], and structure-based methods, such as the Discrete Bubble Model [5], and the Discrete Cluster Model [23,57]. One notable drawback of the TFM in MFIX is the absence of cohesive inter-particle forces, such as electrostatic and van der Waals forces between particles. These forces play a major role in fluidization of strongly cohesive particles in Geldart A and C groups by creating heterogeneous structures, called clusters. According to Li et al. [21], clusters affect the flow significantly by changing the mass and momentum transfers between the gas and solid phases. Many researchers, such as Andrews et al. [1], Agrawal et al. [58], Zhang and Vanderheyden [56], McKeen and Pugsley [26], Yang et al. [55], Ye et al. [51–53], Qi et al. [31], Wang et al. [46], Wang and Li [48], Wang [47], Lu et al. [6,24], Igci et al. [17], and Li et al. [21], believe that clusters are responsible for significant reduction of the interfacial

drag forces between the gas and solid phases. Therefore, dependency of the drag forces on the nature of the attractive interparticle forces plays as important role as the dependency on two other parameters, i.e., the Reynolds number of the flow around particles and the volume fraction of the solid phase in each computational cell. There have been several attempts to improve the performance of the MFIX-TFM code by introducing more complex drag laws, which can consider the effect of subgrid-scale heterogeneous structures in TFM simulations, such as the filtered models of Igci et al. [17] and Milioli et al. [28] and Andrews et al. [1] according to van der Hoef et al. [43] and Wang et al. [47]. However, the constitutive models used in these filtered models were obtained from highly resolved simulations of kinetic theory-based TFM simulations in the absence of the cohesive interparticle forces. This gap can be filled by inclusion of cohesive interparticle forces in the MFIX-TFM code, similar to the inclusion of van der Waals in the MFIX-DEM code (MFIX-2013 Release Notes). In addition, no study has been found in the literature that has implemented the inclusion of the van der Waals forces in the drag laws within the MFIX-TFM code.

DNS has been widely used in high resolution simulation of gas-particle flows in suspension and fluidized beds by researchers such as Ma et al. [25], Cho et al. [7], Xiong et al. [49], and Yin and Sundaresan [54], Garg et al. [11] and Sharma and Patankar [34]. Ma et al. [25] acknowledged the diversity and structural dependence of the drag force on each particle, rather than relying on the entire control volume performed in methods such as TFM. Their analysis, akin to DNS analysis of Xiong et al.

\* Corresponding author. Tel: +1 305 348 6340; fax: +1 305 348 1852.

E-mail addresses: [Gokaltun@fiu.edu](mailto:Gokaltun@fiu.edu), [Gokaltun@gmail.com](mailto:Gokaltun@gmail.com) (S. Gokaltun).

[49], proved that the drag force is significantly different on particles in dilute regions compared to grouped particles.

One useful approach in DNS modeling is the analysis of the flow over fixed assemblies of particles, as practiced by Hill et al. [13,14], van der Hoef et al. [44], Beetstra et al. [2], Yin and Sundaresan [54], and Tenneti and Subramaniam [39]. This approach increases the accuracy and relevance of the information collected. For example, information about field variables, such as the coefficient of drag, and gas and particle velocities can be obtained. Additionally, various different cluster configurations could be analyzed. Cluster differences include: shape, compactness, orientation of the cluster relative to the fluid, spinning speed of the cluster, and various flow-solid relative velocities. A combined particle or cluster resolved DNS analysis coupled with the TFM analysis of the flow could contribute to the improvement of the TFM modeling of the clustering multiphase flow systems. There is also an opportunity for a simulation of the flow on the industrial-scale, using the information obtained in particle or cluster-scale.

Presently, MFIx is a widely known, reliable, and professionally established package for simulation of heat and mass transfer. MFIx accommodates a variety of drag models that can be used in TFM simulation of gas–solid particulate flows. Yet, the direct or indirect addition of models for particle-to-particle, attractive and repulsive forces to the transport equations solved in TFM, or to the available drag laws, is missing. According to Ye et al. [51,52] and Seville et al. [33], these forces could be formulated as  $\vec{F}_{ij}^{(c)} = (AR/6d_{ij}^2) \vec{n}_{ij}$ , where  $F_{ij}^{(c)}$  is the cohesive inter-particle force and  $A$  is the Hamaker constant ( $\approx 10^{-19}$  J) [18],  $R$  is the radius of the monodispersed particles,  $d$  is the surface to surface distance between particles and  $\vec{n}$  is the normal vector pointing from the center of particles  $i$  to the center of the particle  $j$ . Further, they defined a scaling factor,  $\phi = \frac{|U_{min}|}{K_B T} = \frac{AR}{6Z_0} \cdot \frac{1}{K_B \Theta_s}$ , which is the ratio between the interparticle cohesive and destabilizing forces for  $d \leq 100$   $\mu\text{m}$ . In this definition,  $K_B$  is the Boltzmann constant ( $K_B \approx 1$ , [51]),  $Z_0$  is the threshold for particles to be considered as clustered ( $Z_0 \approx 4$  nm, [33]) and  $d$  and  $\Theta_s$  are the diameter and granular temperature of the solid particles. The derivation of equations governing the particle motion can produce a similar quantifying scaling factor, which can indicate the onset of cluster formation. In this analysis, as compared to the cohesion models available in the MFIx-DEM, the scaling factor is an additional factor to be considered for cluster formation, (in addition to the surface to surface particle distances).

Destabilizing forces in the particle–gas systems are mainly due to the particle-to-particle and particle-to-gas interactions. These interactions significantly influence the analysis of particle–gas flows, which has attracted the attention of many researchers, such as Dombrowski and Johns [9], Gidaspow [12], Ding and Gidaspow [12], Cho et al. [7], Benyahia [4], Karimipour and Pugsley [20], and Syamlal et al. [38]. Special attention has been paid to this parameter in the work of Yet et al. [51]. The granular temperature is a measure of the particle fluctuating energy and could be used as a critical parameter to predict the coalescence of particles and break-up of clusters in numerical simulations. MFIx-TFM can solve the transport equation or the algebraic equation, in order to obtain the granular temperature.

In this study, we introduce a cohesive index into the MFIx-TFM code and implement it as a criterion for switching between a Particle-Resolved Direct Numerical-Simulation model, the TGS model, and three existing drag models available in the MFIx code. The rest of the paper is organized as follows. First, the model formulation is presented where the governing equations for the TFM model, the governing equations related to the model of motion of particles leading to our cohesive index and the governing equations of the Gidaspow, Syam–O'Brien, Wen–Yu and TGS drag models are presented. Later, the methodologies for implementing the cohesive index, error calculations and switching between the TGS and other models is presented and followed by the examination of the proposed models in numerical simulations for flow in a fluidized bed. Finally, a conclusion is

drawn on the effectiveness of the proposed model and the authors' perspective of the future work.

## 2. Numerical model

In the TFM, both the gas and the particulate phases are considered as interpenetrating continuous mediums. Complete derivations of the equations governing the two-fluid model can be found in the work of Gidaspow [12]. Here, the equations of the TFM model for flow without phase change and chemical reactions are given by [35] as

$$\frac{\partial(\rho_k \epsilon_k)}{\partial t} + \nabla \cdot (\rho_k \epsilon_k \vec{u}_k) = 0, \quad (1)$$

$$\frac{\partial(\rho_k \epsilon_k \vec{u}_k)}{\partial t} + \nabla \cdot (\rho_k \epsilon_k \vec{u}_k \vec{u}_k) = -\epsilon_k \nabla \rho_k + \epsilon_k \rho_k \vec{g} + \nabla \cdot (\epsilon_k \vec{\tau}_k) + \beta(\vec{u}_l - \vec{u}_k), \quad (2)$$

$$\vec{\tau}_k = [\lambda_k \nabla \cdot \vec{u}_k] \vec{I} + 2\mu_k \left[ \frac{1}{2} \left[ \nabla \vec{u}_k + (\nabla \vec{u}_k)^T \right] - \frac{1}{3} \nabla \cdot \vec{u}_k \vec{I} \right]. \quad (3)$$

Eqs. (1) to (3) show the equations for continuity, momentum balance, and the stress tensor for the phases in TFM, respectively. In these equations,  $\rho$ ,  $\vec{u}$ ,  $\epsilon$ ,  $\vec{g}$ ,  $\vec{\tau}_k$ ,  $\beta$ ,  $\lambda$  and  $\mu$  represent the density, velocity vector, volume fraction, acceleration of gravity, shear stress tensor, momentum exchange coefficient, thermodynamic pressure, second coefficient of viscosity (or bulk viscosity), and the dynamic viscosity of the phases. In addition,  $k$  and  $l$  serve as identifiers for gas and solid phases. However, in Eq. (2), identifiers are phase specific, where if  $k$  refers to one of the phases (e.g., fluid), then  $l$  can only refer to the solid, and vice versa. In this work, the second coefficient of viscosity for the gas phase is set to zero, as suggested by Lu et al. [6,24].

The pressure term for the solid phase,  $p_s$ , is obtained by grouping the gas pressure and the solid phase pressure together, as displayed by Eq. (4).

$$p_s = p_g + p_s. \quad (4)$$

The solid phase pressure is obtained from the granular kinetic model of Ding and Gidaspow [8], as  $p_s = \Theta_s [1 + 2(1 + e_{ss}) \epsilon_s g_{0ss}]$ . Where,  $\Theta_s$  and  $e_{ss}$  represent the granular temperature of the solid phase and particle–particle restitution coefficient, respectively. Here, the  $e_{ss}$  is set to 0.9 according to Jenkins and Zhang [19] and Benyahia [4]. In addition, the solid bulk viscosity, solid shear viscosity, and radial distribution function are given by Samuelsberg and Hjertager [35] as

$$\lambda_s = \rho_s d_p (e_{ss} + 1) \frac{4\epsilon_s^2 \sqrt{\Theta_s g_0}}{3\sqrt{\pi}}, \quad (5)$$

$$\mu_s = \frac{5\sqrt{(\pi\Theta_s)\rho_s d_p}}{48(e_{ss} + 1)g_0} \left[ \left( 1 + \frac{4}{5}(e_{ss} + 1)\epsilon_s g_0 \right)^2 + \left( \frac{4\epsilon_s^2 \rho_s d_p g_0 (1 + e_{ss}) \sqrt{\Theta_s}}{5\sqrt{\pi}} \right) \right], \quad (6)$$

$$g_0 = \frac{3}{5} \left[ 1 - \left[ \frac{\epsilon_s}{\epsilon_{s\max}} \right]^{1/3} \right]^{-1}, \quad (7)$$

respectively. The transport equation for the granular energy is originally derived by Ding and Gidaspow [8]. However, a more complete version is given by Lu et al. [6,24] as

$$\begin{aligned} \frac{3}{2} \left[ \frac{\partial}{\partial t} (\rho_s \epsilon_s \Theta_s) + \nabla \cdot (\rho_s \epsilon_s \vec{u}_s \Theta_s) \right] \\ = (-\epsilon_s p_s \vec{I} + \epsilon_s \vec{\tau}_s) : \nabla \vec{u}_s - \nabla \cdot (k_{\Theta_s} \nabla \Theta_s) - \gamma_{\Theta_s} - 3\beta \Theta_s. \end{aligned} \quad (8)$$

**Table 1**

Proposed drag model scheme using the cohesive index for MFIx-TFM simulations.

New drag model	Criteria
Use TGS	$Ha > Ha\_threshold$
Use an existing model	$Ha \leq Ha\_threshold$

The diffusion coefficient of the granular temperature and the collisional energy dissipation are defined by Eq. (9) and Eq. (10), respectively [35].

$$k_{\theta_s} = \frac{150 \rho_s d_s \sqrt{(\Theta_s \pi)}}{384 (1 + e_{ss}) g_0} \left[ 1 + \frac{6}{5} \varepsilon_s g_0 (1 + e_{ss}) \right]^2 + 2 \rho_s \varepsilon_s^2 d_s (1 + e_{ss}) g_0 \sqrt{\frac{\Theta_s}{\pi}}, \quad (9)$$

$$\gamma_{\theta_s} = 3(1 - e_{ss}^2) \rho_s \varepsilon_s^2 \Theta_s g_0 \left( \frac{4 \sqrt{\Theta_s}}{d_s \sqrt{\pi}} - \nabla \cdot \vec{u}_s \right). \quad (10)$$

According to Ye et al. [52], the translational state of the particulate phase is described by the Newtonian equations of motion (Eq. (11)) for each individual particle in the system.

$$m_i \frac{d^2 \vec{x}_i}{dt^2} = \vec{F}_{ci,i} + \vec{F}_{vdw,i} + \vec{F}_{drag,i} - V_i \nabla p + m_i \vec{g} \quad (11)$$

The terms on the RHS of this equation are the contact force, the van der Waals force, the gas–particle drag force, the force due to pressure gradient in the fluid, and the gravitational force, respectively. In these terms,  $m$  is the mass of the particle,  $V$  is the particle volume,  $\vec{x}$  is the position vector pointing from the center of the particle  $j$  to the center of the particle  $i$ , and  $\vec{g}$  is the vector of acceleration of gravity. Eq. (11) can be rewritten for particle  $j$  with exactly the same properties as the particle  $i$  where, the surfaces of the two particles,  $i$  and  $j$ , are assumed to be in small separation distance from each other. In our approach, since particles are not in a contact, the collisional force term,  $\vec{F}_{ci,i}$ , vanishes from our equation. Later, by considering the small size and separation distance of the particles, with a good estimate, we assume that particles are affected equally by the gas flow and the gravity field variables. Hence, the third, fourth, and the fifth terms on the RHS are assumed equal in magnitude and direction. However, particles  $i$  and  $j$  exchange equal van der Waals forces in opposite directions. Here, we use the

**Table 2**

Governing equations for the existing drag models used for switching procedure.

O'Brien–Syamlal drag model [36–38]	
$\beta = \frac{3\varepsilon_g \varepsilon_p \mu_g}{4V_{rs}^2 d_p} C_{d0} \left( \frac{Re_p}{V_{rs}} \right)  V_g - V_s $	Eq. (20-a)
$V_{rs} = 0.5(A - 0.06Re_p + \sqrt{(0.06Re_p)^2 + 0.12Re_p(2B - A) + A^2})$	Eq. (20-b)
$A = \varepsilon_g^{4.14}$	Eq. (20-c)
$B = \begin{cases} 0.8 \varepsilon_g^{1.28} & \text{for } \varepsilon_g \leq 0.85 \\ \varepsilon_g^{2.65} & \text{for } \varepsilon_g > 0.85 \end{cases}$	Eq. (20-d)
$C_{d0} = (0.63 \sqrt{\frac{Re_p}{V_{rs}}} + 4.8)^2 \times \frac{V_{rs}}{Re_p}$	Eq. (20-e)
Gidaspow drag model [12]	
$\beta = \begin{cases} 50 \frac{\varepsilon_s^2 \mu_g}{d_p^2 \varepsilon_g} + 1.75 \varepsilon_g \frac{\rho_g}{d_p}  V_g - V_s  & \text{for } \varepsilon_g \leq 0.8 \\ 0.75 C_{d0} \frac{\varepsilon_s \varepsilon_p \mu_g}{d_p}  V_g - V_s  \varepsilon_g^{-2.65} & \text{for } \varepsilon_g > 0.8 \end{cases}$	Eq. (21-a)
$C_{d0} = \begin{cases} 0.44 & \text{for } Re \geq 1000 \\ \frac{24}{Re_p} (1 + 0.15 Re_p^{0.687}) & \text{for } Re < 1000 \end{cases}$	Eq. (21-b)
Wen–Yu drag model [45 and 50]	
$\beta = 0.75 C_{d0} \frac{\varepsilon_s \varepsilon_p \mu_g}{d_p}  V_g - V_s  \varepsilon_g^{-2.65}$	Eq. (22-a)
$C_{d0} = \begin{cases} 0.44 & \text{for } Re \geq 1000 \\ \frac{24}{Re_p} (1 + 0.15 Re_p^{0.687}) & \text{for } Re < 1000 \end{cases}$	Eq. (22-b)

**Table 3**

Drag model combinations tested in this study.

Version of the model	Switching procedure	Criteria for switching
AGDSM1	Use TGS	$Ha > Ha\_threshold$
	Use Syam–O'Brien	$Ha \leq Ha\_threshold$
AGDSM2	Use TGS	$Ha > Ha\_threshold$
	Use Wen–Yu	$Ha \leq Ha\_threshold$
AGDSM3	Use TGS	$Ha > Ha\_threshold$
	Use Gidaspow	$Ha \leq Ha\_threshold$

expression of Ye et al. [51] for the van der Waals force between two identical spherical particles and obtain a simplified form for the relative equation of translational motion for particles, as follows

$$m_{eff} \frac{d^2 \vec{x}_{ij}}{dt^2} + \frac{AR_s}{6d^2} = 0. \quad (12)$$

Where,  $\vec{x}_{ij}$  is the vector of instantaneous relative position of the particle  $i$  with respect to the particle  $j$ ,  $m_{eff}$  is the effective mass defined as  $m_{eff} = m_i m_j / (m_i + m_j)$ , and  $A$ ,  $R_s$  and,  $d$  are the Hamaker constant, radius of the particle, and the separation distance between the two particles, respectively. Complete derivation of the governing equations is available in Appendix A.

Later, definition of the granular temperature,  $\Theta = 1/3 \langle \text{particle velocity fluctuation}^2 \rangle$  [12,59], and a short range separation distance within which attractive forces are dominant [51],  $d_0$ , are used to create dimensionless parameters, such as  $\tilde{t} = t \sqrt{\Theta_s} / d_0$  and  $\vec{\tilde{x}}_{ij} = \vec{x}_{ij} / d_0$ , respectively. By defining the vector of relative velocity as  $\vec{V}^{(ij)} = d \vec{x}^{(ij)} / dt$ , we obtain

$$Ha^{-1} \left[ \frac{d\tilde{t}}{d\tilde{p}} \right]^2 \frac{d\vec{V}_{ij}}{d\tilde{t}} + 1 = 0, \quad (13)$$

where,  $\tilde{V}^{(i)} = \vec{V}^{(i)} / \sqrt{\Theta_s}$  and the  $Ha$  parameter is defined as

$$Ha = \frac{A}{\pi \rho d_p^2 d_0 \Theta_s}. \quad (14)$$

In this expression,  $\rho$  is the density of the solid particle,  $d_p$  is the particle diameter,  $d_0$  is the surface to surface cut-off distance, and  $\Theta$  is the granular temperature. The  $Ha$  parameter is the ratio of interparticle cohesive force to the destabilizing force, kinetic energy, acting on each particle in the computational domain. In our TFM simulations, the  $Ha$  parameter can be obtained for each computational node for the

**Table 4**

Set up parameters for MFIx-TFM simulations.

Property	Symbol	Value	Unit
Material	Air and FCC		
Particle diameter	$d_p$	54	$\mu m$
Particle density	$\rho_s$	930	$kg/m^3$
Air viscosity	$\mu_g$	$1.887 \times 10^{-5}$	$Pa \cdot s$
Superficial gas velocity	$U_g$	1.52	$m/s$
Solids mass flux	$G_s$	14.3	$kg/(m^2 \cdot s)$
Single particle terminal velocity	$u_t$	0.077	$m/s$
Minimum fluidization voidage	$\varepsilon_{mf}$	0.4	–
Packing limit	$\varepsilon_{s,max}$	0.63	–
Particle–particle coefficient restitution	$\varepsilon_s$	0.9	–
Particle–wall coefficient restitution	$\varepsilon_w$	0.99	–
Specularity coefficient	$\varphi$	0.0001	–
Initial solids concentration	$\varepsilon_{s,init}$	0.106	–
Riser diameter	$D_t$	0.09	$m$
Riser height	$h$	10.5	$m$
Overall simulation time	$T_{stop}$	20	$s$
Grid size, radial $\times$ axial		$20 \times 150, 40 \times 300, 60 \times 450$	

**Table 5**

Thresholds for solid volume fraction and granular temperature to prevent switching from the standard model to the TGS model.

Assignment	Condition (thresholding)
$Ha = 0$	For $\epsilon_s < \epsilon_{s\_THS}$
$Ha = 0$	For $\Theta_{m\_THS}$

continuous representation of the solid phase. In fact, an increase of this parameter increases the chance of clustering in the domain. This heterogeneity discourages the use of the standard models which are appropriate for non-clustered particles. Therefore, it is appropriate to switch to a DNS-based drag model that can resolve the flow around small-scale structures, such as clusters of particles, more robustly for large values of  $Ha$ . Thus, we use this cohesive index as a criterion for switching between the TGS and other standard drag models. This idea is conceptualized in a new drag model, as illustrated in Table 1 below.

The TGS drag model was developed by Tenneti et al. [39] based on their immersed boundary method of the flow around fixed assemblies of particles (Tenneti and Subramaniam [40]). TGS model with its improved correlation for the gas–solid drag force generates more accurate results for the same ranges of the flow Reynolds number and solid volume fraction compared to its succeeding particle resolved-DNS models. Moreover, TGS model extends the accuracy in DNS modeling of the gas–solid flows to include wider ranges of  $\epsilon_s$  and  $Re_m$ . Theoretically, The TGS model, displayed by Eq. (15), adds two modifications to the single particle-based drag law of Schiller and Naumann [32], which is

displayed by Eq. (16). These terms, defined as  $F_{\epsilon_s}$  and  $F_{\epsilon_s, Re_p}$ , include the pure effect of the solid volume fraction (Eq. 17), and, the combined effect of the Reynolds number and solid volume fraction (Eq. 18), respectively. The outcome from this model is the exchange coefficient defined by Eq. (19).

$$F(\epsilon_s, Re_p) = \frac{F_{isol}(Re_p)}{(1-\epsilon_s)^3} + F_{\epsilon_s}(\epsilon_s) + F_{\epsilon_s, Re_p}(\epsilon_s, Re_p), \quad (15)$$

$$F_{isol}(Re_p) = 1 + 0.15Re_p^{0.687}, \quad (16)$$

$$F_{\epsilon_s}(\epsilon_s) = \frac{5.81\epsilon_s}{(1-\epsilon_s)^3} + 0.48 \frac{\epsilon_s^{1/3}}{(1-\epsilon_s)^4}, \quad (17)$$

$$F_{\epsilon_s, Re_p}(\epsilon_s, Re_p) = \epsilon_s^3 Re_p \left( 0.95 + \frac{0.61\epsilon_s^{1/3}}{(1-\epsilon_s)^2} \right), \quad (18)$$

$$\beta = 18 \mu_g \epsilon_g \epsilon_s \frac{F(\epsilon_s, Re_p)}{d_p^2}. \quad (19)$$

Table 2 shows different versions of the exchange coefficient ( $\beta$ ) in Eqs. (2) and (8), which are used in the existing drag models in MFIX. In addition, Table 3 shows the description of different versions of the drag model scheme labeled as AGDSM1, AGDSM2, and AGDSM3, as proposed in this work.

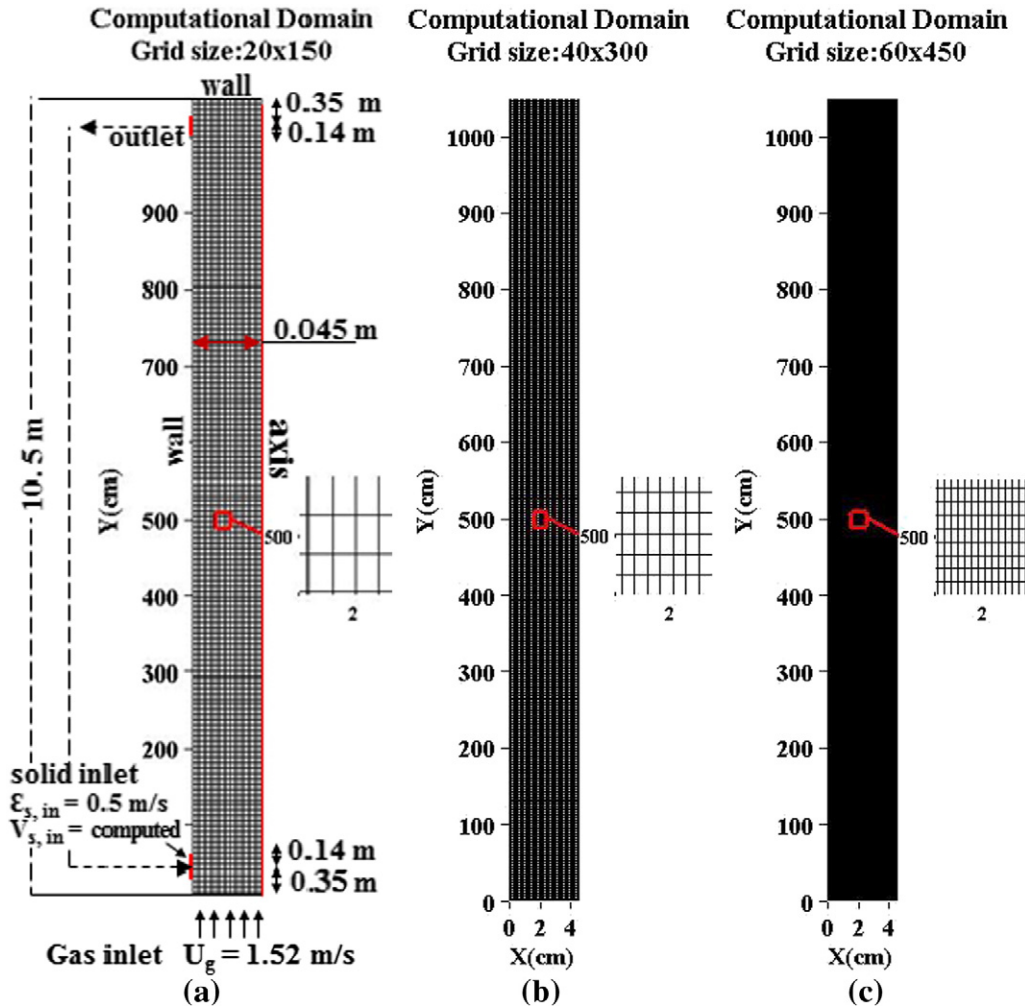


Fig. 1. Computational domain and boundary conditions used for MFIX-TFM fluidized bed flow simulations, (a)  $20 \times 150$ , (b)  $40 \times 300$ , (c)  $60 \times 450$ .



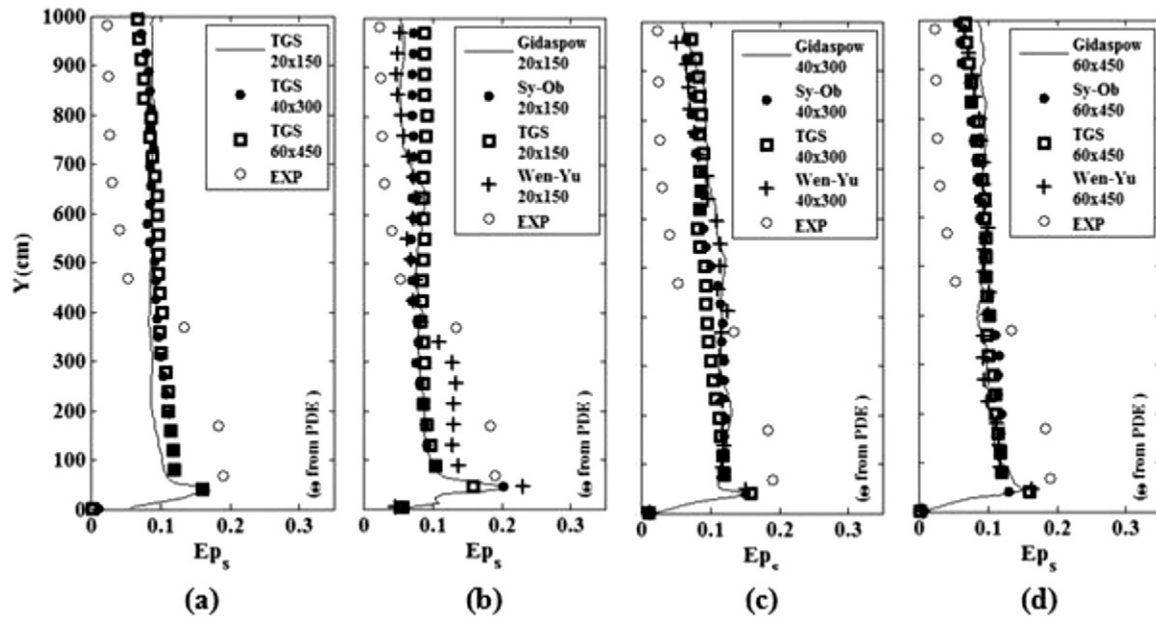


Fig. 2. Profile of solid volume fraction along the riser of the fluidized bed, MFIx-TFM results with TGS and existing drag models on three computational grid sizes.

### 3. Simulation methodology

The performance of each individual drag model was evaluated initially for a 20-second simulation of the flow in a circulating fluidized bed. We obtained permission from Li and Kwauk [22] and Hong et al. [15] to use their experimental and numerical data in our analysis, respectively. Hong et al. [15] showed that utilization of the homogenous drag model, the correlation of Gidaspow [12], fails to produce accurate grid-independent results. Similar failure was reported by Lu et al. [6, 24] and Benyahia [3,4] with the Ergun/Wen and Yu drag correlation [10,45]. In the present study, similar to the work of Hong et al. [15], we used the laminar flow assumption for the air and the transport equation of the granular temperature for fluctuations of the solid phase. However, in order to improve the accuracy in all simulation cases, we assigned the equation of the state for calculation of the air density. Settings are displayed in Table 4.

Additionally, computational results obtained in the last 100 time steps were time and space-averaged on each cross section along the riser of the fluidized bed. The profile of the solid volume fraction was plotted against the available experimental data points. A computer script was used to interpolate the numerical results for specific heights of the riser, where data points from the experiment of Li and Kwauk [22] were available. Then, the maximum of the deviation of the numerical data points from the corresponding experimental data points was calculated by Eq. (23). Further, for each drag model used in this study, an absolute average percentage deviation (AAPD) value, as shown by Eq. (24) was calculated.

$$\text{Err}_{\max} = \text{Max}(|f_{\text{exp}}(\lambda) - f_{\text{sim}}(\lambda)|) \quad (23)$$

$$\text{AAPD} = \text{Err}_{\text{avg}}(\%) = \frac{100}{N} \times \sum_{\lambda=1}^N (|f_{\text{exp}}(\lambda) - f_{\text{sim}}(\lambda)| / f_{\text{exp}}(\lambda)) \quad (24)$$

The equations given above,  $f_{\text{sim}}$  and  $f_{\text{exp}}$  are numerical and experimental data point values at locations along the riser of the experimental facility, respectively. The parameter  $\lambda$  shows the index of the locations and AAPD-9 refers to the label used for the AAPD value calculated using a total of nine (i.e.,  $N = 9$ ) data points in our initial error calculations. In addition, a polynomial function was fitted to the nine experimental data points in order to create a profile with significantly more

number of points for the error analysis. Thus, the target parameters, such as the correlation values between the numerical and experimental profiles, i.e.,  $R^2$ , and the AAPD, are calculated for 150 points along the riser. Eq. (25) shows the expression used for calculation of the  $R^2$  value for each constituent and hybrid model.

$$(R^2)_{\text{model}} = 1 - \frac{\sum_{i=1}^N \left( Y_{i,\varepsilon_s} - \frac{1}{N} \sum_{i=1}^N Y_{i,\varepsilon_s} \right)^2}{\sum_{i=1}^N (Y_{i,\varepsilon_s} - f_{i,\varepsilon_s})^2} \quad (25)$$

This criterion was used for the overall comparison between the simulation results and the experimental data. In this definition  $N$ ,  $Y_{i,\varepsilon_s}$  and  $f_{i,\varepsilon_s}$  indicate the total number of data points, values of  $\varepsilon_s$  on the polynomial fit, and the values of  $\varepsilon_s$  on the numerical profile of each drag model, respectively.

The improvement to each constituent model was calculated by comparing the  $\text{Err}_{\max}$ ,  $R^2$  and AAPD values before and after using the model in our hybrid schemes. Eqs. (26)–(31) show the expressions used for calculation of these improvements. For brevity, the subscript notations used in Eqs. (29) and (30), i.e., constituent and hybrid, follow the same indexing pattern as used in Eqs. (26) to (29)

$$(\text{imp. Err}_{\max})_{\text{Gidaspow}} = 100 \times \frac{|(\text{Err}_{\max})_{\text{Gidaspow}} - (\text{Err}_{\max})_{\text{AGDSM3}}|}{(\text{Err}_{\max})_{\text{Gidaspow}}} \quad (26)$$

$$(\text{imp. Err}_{\max})_{\text{SY-O'B}} = 100 \times \frac{|(\text{Err}_{\max})_{\text{SY-O'B}} - (\text{Err}_{\max})_{\text{AGDSM1}}|}{(\text{Err}_{\max})_{\text{SY-O'B}}} \quad (27)$$

Table 6

Error in numerical simulation compared to available experimental data of [22] for computational grid size of  $20 \times 150$ .

Simulation case	Max. error	Avg. error (%)
Hong et al. (date)	0.0773	166
Syam-O'Brien	0.0954	106
Gidaspow	0.0959	93
Wen-Yu	0.0545	77
TGS	0.0918	143

**Table 7**  
Variation of the thresholds in the AGDSM models.

Mode-1		Mode-2	
Parameter	Threshold value	Parameter	Threshold value
$\varepsilon_{s\_TGS}$	0.02	$\varepsilon_{s\_TGS}$	$1 \times 10^{-3}$
$\Theta\_TGS$	0.0008 (cm <sup>2</sup> /s <sup>2</sup> )	$\Theta\_TGS$	$1 \times 10^{-16}$ (cm <sup>2</sup> /s <sup>2</sup> )
Ha_TGS	$[1 \times 10^{-5} - 1]$	Ha_TGS	$[1 \times 10^{-10} - 0.1]$

$$(\text{imp.Err}_{\text{max}})_{\text{Wen\_Yu}} = 100 \times \frac{|(\text{Err}_{\text{max}})_{\text{Wen\_Yu}} - (\text{Err}_{\text{max}})_{\text{AGDSM2}}|}{(\text{Err}_{\text{max}})_{\text{Wen\_Yu}}} \quad (28)$$

$$(\text{imp.Err}_{\text{max}})_{\text{TGS}} = 100 \times \frac{|(\text{Err}_{\text{max}})_{\text{TGS}} - (\text{Err}_{\text{max}})_{\text{AGDSM3}}|}{(\text{Err}_{\text{max}})_{\text{TGS}}} \quad (29)$$

$$(\text{imp.AAPD})_{\text{constituent}} = 100 \times \frac{|(\text{AAPD})_{\text{constituent}} - (\text{AAPD})_{\text{hybrid}}|}{(\text{AAPD})_{\text{constituent}}} \quad (30)$$

$$(\text{imp.R}^2)_{\text{constituent}} = 100 \times \frac{|(R^2)_{\text{constituent}} - (R^2)_{\text{hybrid}}|}{(R^2)_{\text{constituent}}} \quad (31)$$

Thresholding constitutes an important feature of all proposed versions of the AGDSM model. Table 5 illustrates two extra threshold values,  $\varepsilon_{s\_TGS}$  and  $\Theta\_TGS$ , that must be assigned, in addition to the threshold for the Ha parameter. This strategy eliminated the possibility of singularity in Ha calculations in very dilute regions of the domain, where granular temperature was extremely small. Moreover, for cells with extremely small values of granular temperature, no switching operations were executed in the program.

The optimum values for the variables listed in Table 5 are obtained by best practices. Initially, relatively small values were assigned to threshold values, which resulted in a limited variation in numerical simulation. Later, extremely small values were selected for these variables, which resulted in a significant change in results and in some cases, a significant improvement in numerical results were obtained. The Ha\_TGS parameter was examined in a wide range for all three proposed versions of the drag model in order to find the optimum value.

#### 4. Simulation results

Fig. 2 illustrates the results obtained with the TGS drag model and the other existing drag models on three different computational grids (See Fig. 1). Fig. 2(a) illustrates the grid independency study with the TGS drag model where the computational grid (40 × 300) was found to be optimum. It was observed that when the existing drag models or the TGS model were used alone, the solid volume fraction profile in

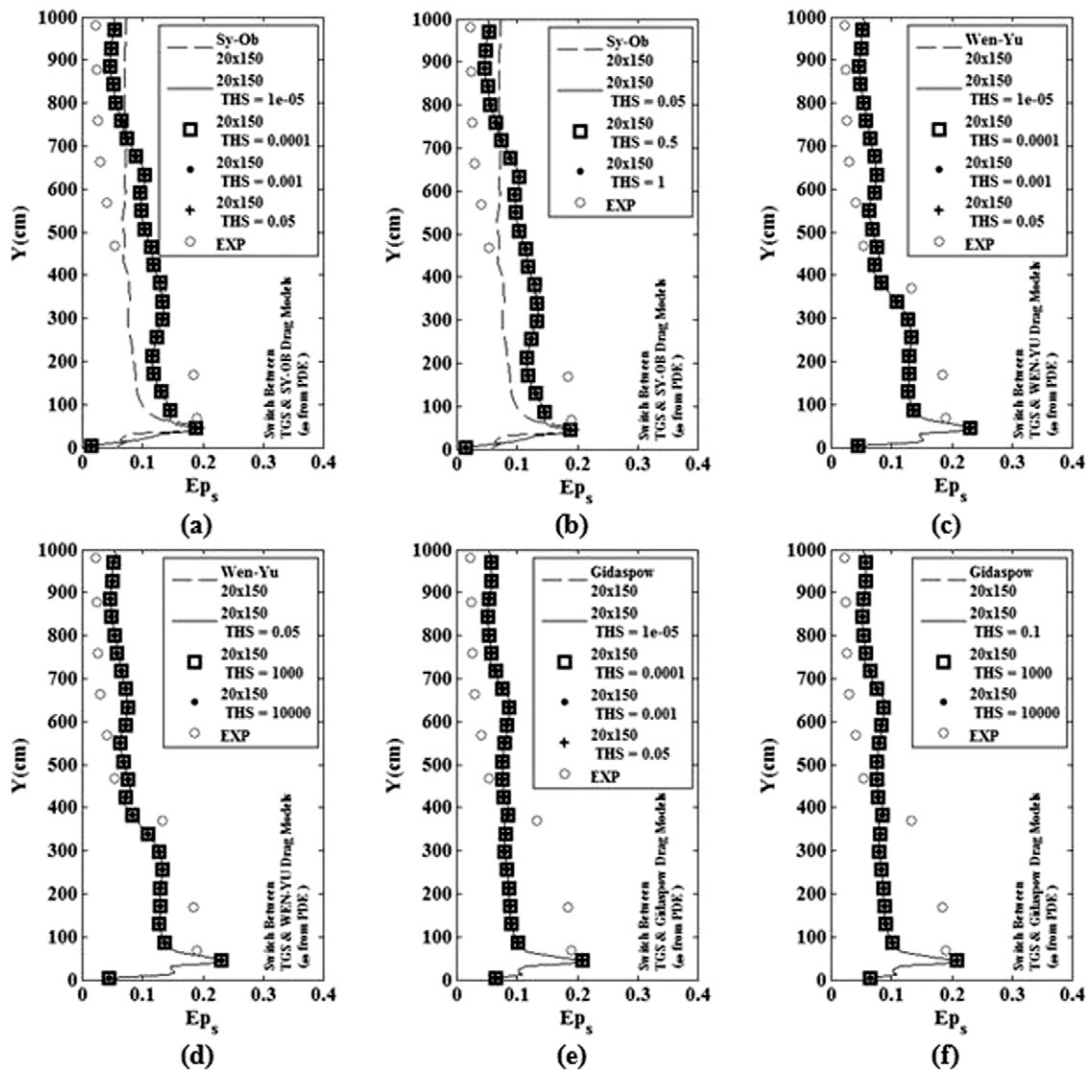


**Fig. 3.** Switching effects in the three versions of the AGDSM model on time and area-averaged profile of the solid volume fraction along the riser against variation of the Ha\_TGS.

the riser showed significant deviation from the experimental data given by Li and Kwauk [22]. Fig. 2(d) shows that all models produce very similar results with the increase of the computational grid size, and these results are in good agreement with the simulation results obtained by Hong et al. [15], where they used the Gidaspow drag model in their simulation of the same flow.

Table 6 shows the maximum and relative errors in the simulation results for the computational grid size of  $20 \times 150$ . The maximum and minimum values for errors were observed in the cases with the TGS

and Wen–Yu correlations, respectively. The results are comparable to the simulation results obtained by Hong et al. [15] for the same geometry and boundary conditions. Further, in order to evaluate the sensitivity of the AGDSM versions to the threshold values,  $\varepsilon_{s\_THS}$  and  $\Theta\_THS$ , these parameters were varied according to the modes given in Table 7.

Fig. 3 shows the effect of switching operations on simulation results under the constraints of the first mode, as explained in Table 7. In this figure, the immediate observation from Fig. 3(a–b) is that, for various values of the  $Ha\_THS$  parameter and the fixed values of  $\varepsilon_{s\_THS}$  and

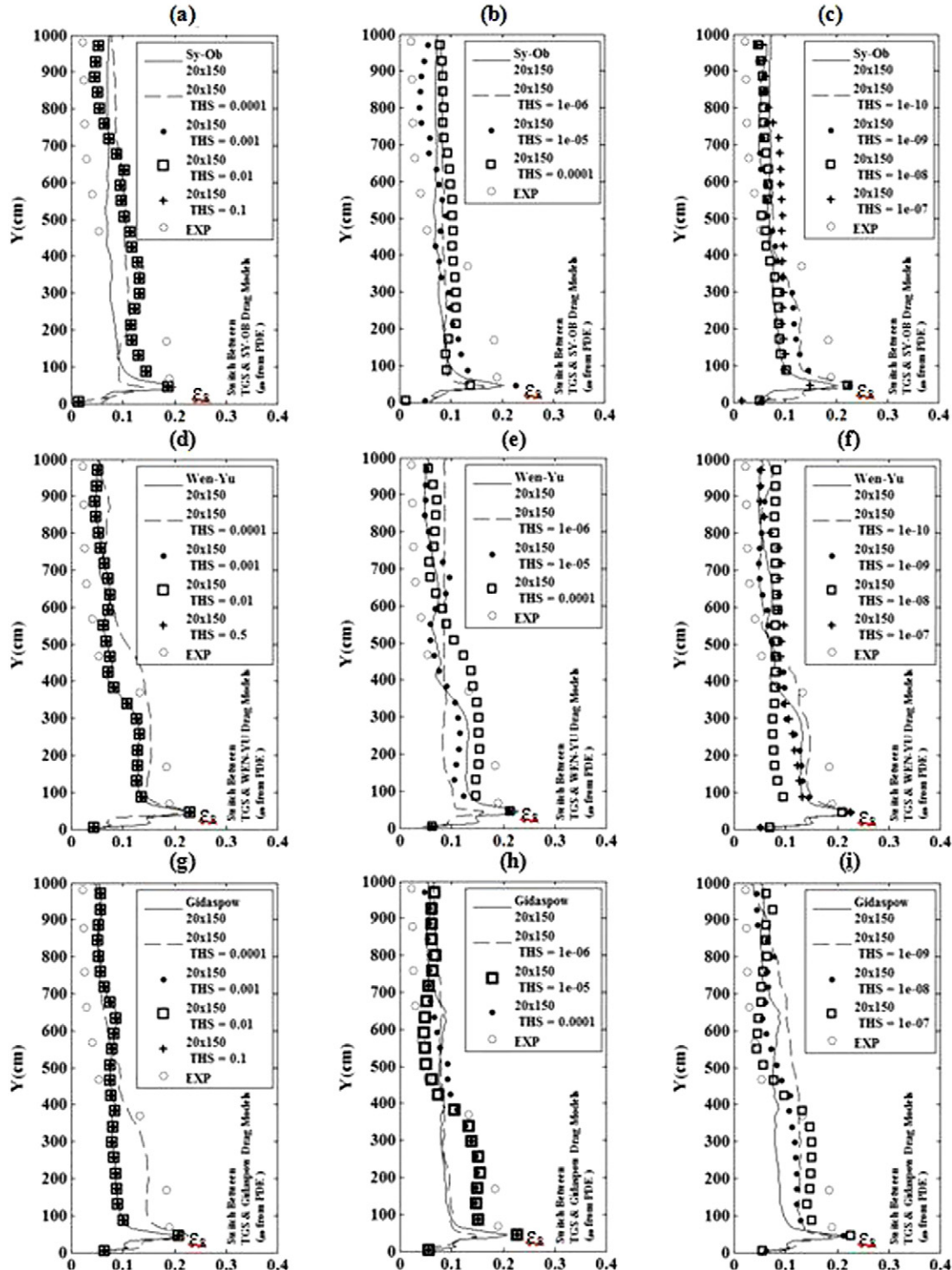


Fig. 4.  $\varepsilon_s$  profile from MFIX-TFM simulations for various values of  $Ha\_THS$ ; (a to c) represent AGDSM1, (d to f) represent the AGDSM2, and (g to i) represent the AGDSM3.



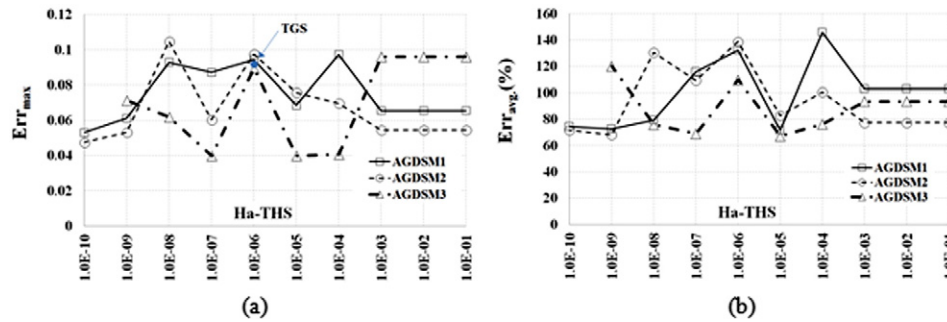


Fig. 5. Error in TFM simulation for three versions of the proposed drag model, maximum of error on the left and averaged relative error on the right.

$\Theta_{\text{THS}}$ , a significant alteration in the solid volume fraction profile occurred. However, identical results were obtained for the  $\text{Ha}_{\text{THS}}$  parameter in a broad range of variation (e.g.,  $[1 \times 10^{-5} \text{ to } 1]$ ). In addition, improvement of the numerical results, in terms of deviation from the experimental data, was limited to only small portions of the computational domain in high and low sections of the riser.

Further, Fig. 3(c–f) show that the effect of filtration by the model constraints is more pronounced for AGDSM2 and AGDSM3 versions of the proposed model. According to Fig. 3(c–d) and (e–f) for the AGDSM2 and AGDSM3 models, respectively, no alteration of the results was observed in a significantly wider range of the  $\text{Ha}_{\text{THS}}$  parameter (e.g.,  $[1 \times 10^{-5} \text{ to } 1 \times 10^4]$ ). In fact, the extremely conservative nature of the filtration procedure, Table 5, accounts for the unnecessary elimination of switching operations in the regions where relatively large values of  $\text{Ha}$  were detected. This observation helps to understand that although the onset of the changes in the simulation results of the AGDSM1 model, occurred at large values of the threshold ( $\text{Ha}_{\text{THS}} = 0.05$ ), the loss of the sensitivity to smaller values of the  $\text{Ha}_{\text{THS}}$  in our modeling could be overcome by significant reduction of the values for the  $\Theta_{\text{THS}}$  and  $\varepsilon_{\text{sTHS}}$  parameters (Mode 2 in Table 7). Here we refer to this treatment as simulation with relaxed constraints and we have shown that this treatment was effective for all versions of the proposed drag model.

#### 4.1. Simulation results with relaxed constraints

Simulation results with relaxed constraints, introduced as mode 2 in Table 7, are displayed in Fig. 4 for the AGDSM1, AGDSM2 and AGDSM3

versions. For the AGDSM1 model, Fig. 4(a) shows an identical  $\varepsilon_{\text{s}}$  profile for  $0.1 \leq \text{Ha}_{\text{THS}} < 0.0001$ . According to Fig. 4(b–c), the onset of the ongoing changes occurred at  $\text{Ha}_{\text{THS}} = 1 \times 10^{-4}$  and significant improvements were observed for  $\text{Ha}_{\text{THS}} = 1 \times 10^{-5}$ ,  $\text{Ha}_{\text{THS}} = 1 \times 10^{-9}$ , and  $\text{Ha}_{\text{THS}} = 1 \times 10^{-10}$ . However, remarkably large deviations from the experimental profile are observed for  $1 \times 10^{-6} \leq \text{Ha}_{\text{THS}} \leq 1 \times 10^{-8}$ , where the AGDSM1 version almost regenerated the  $\varepsilon_{\text{s}}$  profile of the TGS model at  $\text{Ha}_{\text{THS}} = 1 \times 10^{-6}$ .

The AGDSM2 model, as shown in Fig. 4(d), reproduced the original  $\varepsilon_{\text{s}}$  profile of the Wen–Yu model for  $0.5 \leq \text{Ha}_{\text{THS}} < 0.0001$ . Here, unlike the AGDSM1 model, the onset of the changes occurred at  $\text{Ha}_{\text{THS}} = 1 \times 10^{-4}$  and we observed a dynamic variation of results after this threshold value. Here, consecutive increase and decrease of the deviations from the experimental results are observed with the reduction of the  $\text{Ha}_{\text{THS}}$ . In addition, the AGDSM2 version almost regenerated the  $\varepsilon_{\text{s}}$  profile of the TGS model at two threshold values, e.g.,  $\text{Ha}_{\text{THS}} = 1 \times 10^{-6}$  and  $\text{Ha}_{\text{THS}} = 1 \times 10^{-8}$ . However, significant improvements in the agreement with the experimental values were obtained for the  $\text{Ha}_{\text{THS}} = 1 \times 10^{-9}$  and  $\text{Ha}_{\text{THS}} = 1 \times 10^{-10}$ .

The AGDSM3 model, as shown in Fig. 4(g), reproduced the original  $\varepsilon_{\text{s}}$  profile of the Gidaspow model for  $0.1 \leq \text{Ha}_{\text{THS}} < 0.0001$ . Similar to the AGDSM2 version, we observed a dynamic variation of results after the  $\text{Ha}_{\text{THS}} = 1 \times 10^{-4}$ . Further, Fig. 4(g–i) shows consecutive increase and decrease of the deviations of the numerical results from the experimental results and the model almost reproduced the original  $\varepsilon_{\text{s}}$  profile of the TGS model for the intermediate value of the threshold (e.g.,  $\text{Ha}_{\text{THS}} = 1 \times 10^{-6}$ ). However, significantly better agreements

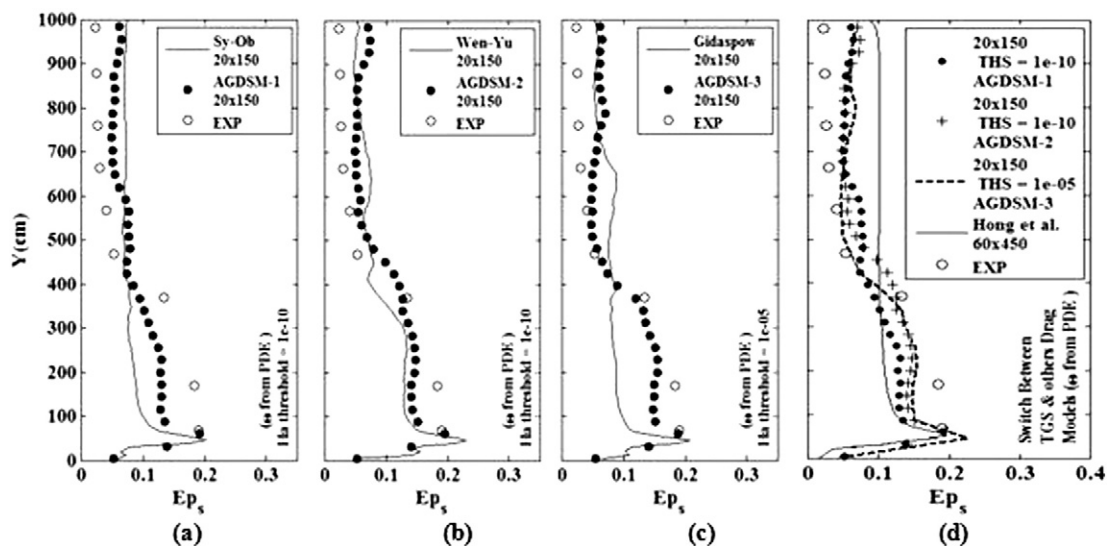


Fig. 6. Optimal MFIX-TFM simulations by versions of the AGDSM model, (a) to (c) are versions of the AGDSM model versus corresponding standard models, (d): best result from AGDSM1–3 versions and the profile of [15].



**Table 8**

Error calculations and best improvements for different versions of the AGDSM model.

Simulation case	Err. <sub>max</sub>	AAPD-9 <sup>a</sup> (%)	AAPD-fit <sup>b</sup> (%)	R <sup>2</sup>	imp. Err. <sub>max</sub> (%)	imp_AAPD (%)	imp_R <sup>2</sup> (%)
[15]	0.0773	166.1	138.5	0.557	–	–	–
Syam–O'Brien	0.0954	106.2	100.7	0.789	44.5	32.0	23.2
Gidaspow	0.0959	93.5	87.9	0.735	58.4	26.4	30.1
Wen–Yu	0.0545	77.4	71.0	0.956	12.9	10.5	1.12
TGS	0.0918	143.1	132.4	0.410	56.5	51.14	133.3
AGDSM1 <sup>c</sup>	0.0531	74.5	68.4	0.973	–	–	–
AGDSM2 <sup>d</sup>	0.0474	71.6	63.6	0.966	–	–	–
AGDSM3 <sup>e</sup>	0.0399	67.2	64.7	0.956	–	–	–

<sup>a</sup> 9-point absolute average percent deviation.<sup>b</sup> Absolute average percent deviation using the 4th order polynomial fit.<sup>c</sup> Ha\_THS =  $1 \times 10^{-10}$ .<sup>d</sup> Ha\_THS =  $1 \times 10^{-10}$ .<sup>e</sup> Ha\_THS =  $1 \times 10^{-5}$ .

with the experimental values were obtained for the  $\text{Ha\_THS} = 1 \times 10^{-5}$  and  $\text{Ha\_THS} = 1 \times 10^{-7}$ .

Further, to improve our error analysis, we plotted the profiles of the maximum and relative errors as displayed in Fig. 5(a) and (b), respectively. Here, we noticed a similarity between the profiles of the maximum and the relative errors for each version of the proposed drag model. Fig. 5(a) shows that the maximum improvements for the AGDSM1, AGDSM2, and AGDSM3 happened at  $\text{Ha\_THS} = 1 \times 10^{-10}$ ,  $\text{Ha\_THS} = 1 \times 10^{-10}$ , and  $\text{Ha\_THS} = 1 \times 10^{-5}$ , respectively. In addition, Fig. 5(a–b) shows that no consistent trend of reduction or escalation of error against values of the Ha-THS parameter could be traced for all proposed versions of the AGDSM model. Moreover, the models did not develop similar patterns of variation for the profiles of  $\text{Err}_{\text{max}}$  and  $\text{Err}_{\text{avg}}$  errors. Our observation is that perturbations on the error profiles start at  $\text{Ha\_THS} = 1 \times 10^{-3}$  for all AGDSM versions and all models approached the  $\text{Err}_{\text{max}}$  value of the TGS model at  $\text{Ha\_THS} = 1 \times 10^{-6}$  (Fig. 5(a)).

Another observation from Fig. 5(a–b) is that the level of error associated with the AGDSM3 model is significantly lower than the other two models for  $1 \times 10^{-8} \leq \text{Ha\_THS} < 1 \times 10^{-4}$ . In other words, switching between the TGS and the Gidaspow drag models could excellently serve the objective of the present research, which is to improve the performance of the existing standard drag modes through a combination with a DNS-based drag model.

Fig. 6 illustrates a thorough comparison between the best results obtained by our proposed hybrid models and their corresponding constituent standard drag model. We first demonstrated in Fig. 6(a–c) that all hybrid models significantly outperformed their corresponding constituent standard drag model. According to Fig. 6(c), the most effective switch operations were performed by the AGDSM3 model.

The error values shown in the Table 8 show that the smallest values of 9-point maximum error and AAPD values calculated using Eqs. (23) and (24) were obtained for the AGDSM3 model under optimal conditions. However, in our analysis with a 4th order polynomial fit with a high fit quality of  $R^2 \approx 0.98$  to the experimental data points, as shown in Fig. 7, a slightly smaller values of AAPD was observed for the AGDSM2 model version. In a similar fashion, the largest 9-point  $R^2$  values was obtained for the AGDSM3 model version, while this model version possessed the second largest  $R^2$  values after the AGDSM2 model version for the polynomial fit. For brevity, the 9-point  $R^2$  values are not shown in the Table 8.

Table 8 also shows the results of our error and  $R^2$ -improvement analysis. Accordingly, all hybrid models used in this study demonstrated high correlation values ( $R^2 \geq 0.95$ ) with the experimental profile. In the case of standard drag models used in this study, the best improvements in terms of maximum-error (%58.4) and  $R^2$ -value (%30.1) were obtained for the Gidaspow drag model. In addition, we were able to improve the results of the Syam–O'Brien drag model in terms of AAPD criterion for the largest improvement value of 32%. This accomplishment is

significant since this improvement was obtained without activating the cluster-related correction parts of the Syam–O'Brien drag subroutine in the MFIX.

In addition, it is possible to make qualitative comparisons between profiles of solid volume fraction in Fig. 6(d) and quantitative comparison between the error and  $R^2$  values on the first and the last three rows of the Table 8. These comparisons reveal the improved performance of all proposed AGDSM model versions in optimal conditions over the results reported by Hong et al. [15] where the Gidaspow model was used on a significantly finer computational grid ( $60 \times 450$ ). The purpose of this comparison is to show that significantly better computational results could be obtained by only combining the non-structured based drag models with the particle resolved-DNS TGS drag model, and without a need for refining the computational grid size.

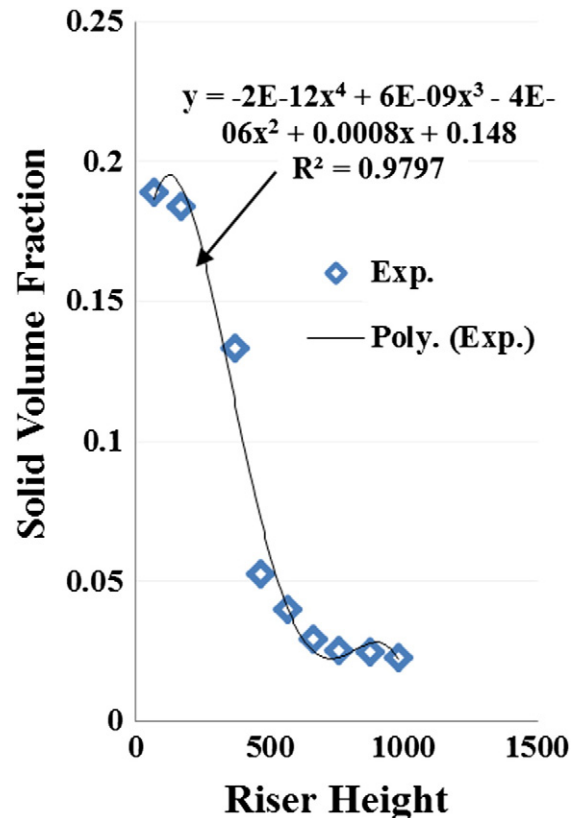


Fig. 7. Fourth-order fit to the experimental data of [22] used for the calculation of  $R^2$  and AAPD values.

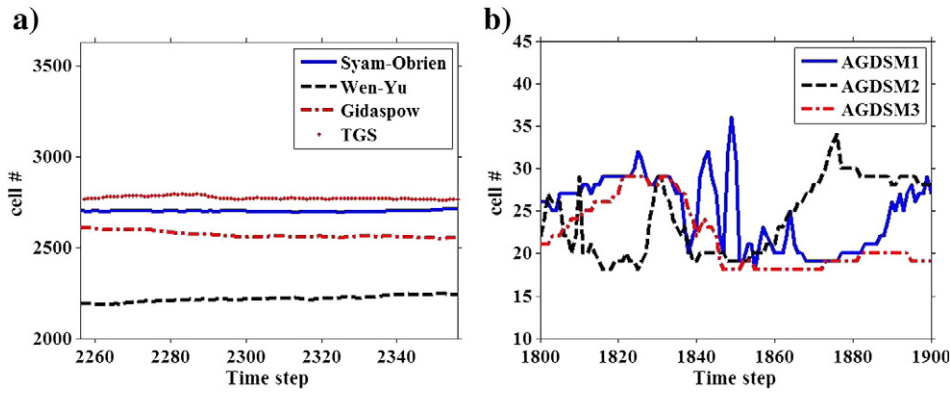


Fig. 8. Frequency of switch operations. (a) Constituent drag models, (b) proposed AGDSM model versions in optimal cases.

#### 4.2. Switching frequency and improvements in AGDSM model versions

Results shown earlier in Fig. 5 indicates an unrecognizable relation between the variation of error and the value of the Ha-THS parameter. The switching mechanism between constituent drag models, as explained earlier in Table 1, is controlled by two parameters, Ha and Ha-THS. Therefore, the results listed in Table 8 encouraged us to explore the relation between the improvements for the proposed versions of the AGDSM model and the switching frequencies occurred in the simulations.

For this purpose, we first calculated the number of the computational cells which met the criteria of switching for all proposed hybrid drag versions. In this method, the frequency of switching operations for AGDSM3 under the best condition (i.e.,  $Ha-THS = 1 \times 10^{-5}$ ) was the number of cells that met the condition of  $Ha > 1 \times 10^{-5}$  and similar definition was used for the AGDSM2 and AGDSM3 versions with  $Ha-THS = 1 \times 10^{-10}$ . For the constituent models, we calculated the number of the computational cells which could potentially meet the switching criterion of  $Ha > 1 \times 10^{-10}$ . The importance of investigation about these criteria was to evaluate the potential of further modification to both the constituent and hybrid drag models based on the relative strangeness of cohesive forces, i.e., cluster formation.

Fig. 8 shows the potential of further modification to all drag models used in this study. These results show significant differences between the constituent models, presented in Fig. 8(a), and the proposed hybrid model versions, presented in Fig. 8(b). Surprisingly, there is a direct relation between the improvement to the AAPD values listed in the Table 8 and the potential modifications shown in Fig. 8(a). In better words, the TGS model with the highest AAPD values, i.e., %132.4, required the most number of switching operation, i.e., 2774, and possessed the highest level of overall modification (imp-AAPD), i.e., % 51.14. In a similar fashion, the Wen-Yu model with the lowest AAPD, required the smallest number of operations and possessed the least level of AAPD improvements. Based on these observations, significant modifications shown in Fig. 6 and Table 8 can be explained by the significant changes which occurred to the constituent models through switching operations between the standard models and the TGS model; however, the relation between the large number of switching operations required for the Wen-Yu model and the level of modification to this model, as described by Table 8, necessitates more attention to be given to the effectiveness of switching operations for different models. Therefore further research is necessary to investigate about the relation between cohesive index and field variables, such as granular temperature of the solid phase and drag force coefficients. (See Fig. A-1.)

#### 5. Conclusions

In this paper, we have demonstrated that TFM simulations of the air-FCC flow could not produce accurate results using the original

form of three existing standard drag models in the MFI package (i.e., Syam-O'Brien, Gidaspow and Wen-Yu models) and the TGS model, as a particle resolved DNS drag model. On the other hand, combining a standard drag model with the TGS model, under optimized conditions and based on a switching mechanism, was proved to be a useful method to significantly improve the accuracy of the numerical results. In this approach, the switching mechanism proved to be exceptionally sensitive to the variation of the threshold values of the cohesive index, Ha-THS. A direct relation between the error improvements and the frequency of switch operations in the proposed models is recognized. Consequently, models with more numerical error demanded more switching operations and experienced more modifications. However, improvements to the constituent models must be considered together with the quality of the switch operations. This can lead to establishment of an accurate relation between the drag force and the cohesive index, hence a more comprehensive drag force model wherein the cohesive index is explicitly incorporated into its formulation. In conclusion, the proposed approach was observed to be successful for all the three drag model versions under optimal conditions, where a maximum of almost 60% improvement in accuracy of simulation results was obtained for the Gidaspow model. Therefore, a direct or indirect implementation of particle clustering and ensuing modifications in the TFM approach is necessary to be practiced for gas-solid flows under the influence of cohesive interparticle forces.

#### Acknowledgments

Funding for this work was provided by the Department of Energy's National Energy Technology Laboratory under grant number DE-FE0007260.

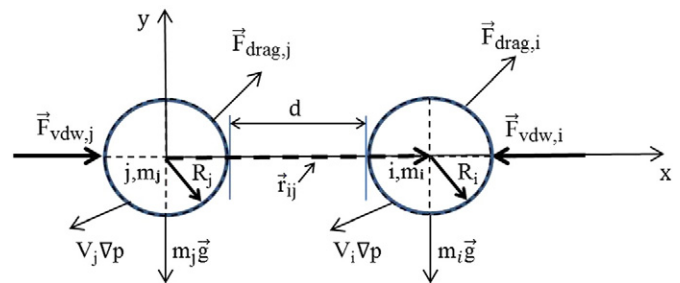


Fig. A-1. Representation of the van der Waals force, the gas-particle drag force, the force due to pressure gradient in the fluid, and the gravitational force acting on two spherical particles with equal radius.

## Appendix A. Relative equation of motion of particles

For particle i:

$$m_i \frac{d^2 \vec{x}_i}{dt^2} = \vec{F}_{c,i} + \vec{F}_{vdw,i} + \vec{F}_{drag,i} - V_i \nabla p + m_i \vec{g} \quad (A.1)$$

For particle j:

$$m_j \frac{d^2 \vec{x}_j}{dt^2} = \vec{F}_{c,j} + \vec{F}_{vdw,j} + \vec{F}_{drag,j} - V_j \nabla p + m_j \vec{g} \quad (A.2)$$

$$\vec{F}_{c,i} = \vec{F}_{c,j} = 0 \quad (A.3)$$

and

$$\vec{F}_{drag,i} = \vec{F}_{drag,j} \quad (A.4)$$

$$V_i \nabla p = V_j \nabla p \quad (A.5)$$

$$m_i \vec{g} = m_j \vec{g} \quad (A.6)$$

$$\vec{F}_{vdw,i} = -\vec{F}_{vdw,j} \quad (A.7)$$

Fig. A-1 shows the schematic of the particles with small separation distance from each other under the effect of the van der Waals force, the gas–particle drag force, the pressure gradient in the fluid, and the gravitational force. Subtraction of Eq. (A.2) from Eq. (A.1) results in cancellation of some of the terms and the following expression is obtained:

$$\frac{d^2 (\vec{x}_i - \vec{x}_j)}{dt^2} = \left( \frac{1}{m_i} \vec{F}_{vdw,i} - \frac{1}{m_j} \vec{F}_{vdw,j} \right) \quad (A.8)$$

where for the cohesive inter-particle force, we adopt the Hamaker expression [60] for two spheres, given by the following equation:

$$\left| \vec{F}_{vdw,ij}(d) \right| = \frac{A}{3} \frac{2R_i R_j (d + R_i + R_j)}{[d(d + 2R_i + 2R_j)]^2} \times \left[ \frac{d(d + 2R_i + 2R_j)}{(d + 2R_i + 2R_j)^2 - (R_i - R_j)^2} - 1 \right]^2 \quad (A.9)$$

In this equation, A is the Hamaker constant, R is the radius of the particle and d is the surface-to-surface distance between the two particles, i and j. This expression simplifies to  $\vec{F}_{vdw,ij}(d) = (AR / 6d_{ij}^2) \vec{n}_{ij}$  for two sphere of the same diameter. Later, by placing the frame of reference on the particle j, and replacing the  $d_{ij}$  with the distance d, in Fig. (A-1), Eq. (A.8) can be reformatted as

$$\left( \frac{m_i m_j}{m_i + m_j} \right) \frac{d \vec{V}_{rel}}{dt} + \frac{AR}{6d^2} = 0. \quad (A.10)$$

## References

- [1] A.T. Andrews IV, P.N. Loezos, S. Sundaresan, Coarse-grid simulation of gas–particle flows in vertical risers, *Ind. Eng. Chem. Res.* 44 (16) (2005) 6022–6037.
- [2] R. Beetstra, M.A. Van Der Hoef, J.A.M. Kuipers, Drag force of intermediate Reynolds number flow past mono- and bidisperse arrays of spheres, *AIChE J.* 53 (2) (2007) 489–501.
- [3] S. Benyahia, Verification and validation study of some polydisperse kinetic theories, *J. Chem. Eng. Sci.* 63 (23) (2008) 5672–5680.
- [4] S. Benyahia, Analysis of model parameters affecting the pressure profile in a circulating fluidized bed, *AIChE J.* 58 (2) (2012) 427–429.
- [5] G.A. Bokkers, J.A. Laverman, M. van Sint Annaland, J.A.M. Kuipers, Modelling of large-scale dense gas–solid bubbling fluidized beds using a novel discrete bubble model, *J. Chem. Eng. Sci.* 61 (17) (2006) 5590–5602.
- [6] Bona Lu, Wei Wang, Jinghai Lia, Searching for a mesh-independent sub-grid model for CFD simulation of gas–solid riser flows, *J. Chem. Eng. Sci.* 64 (15) (2009) 3437–3447.
- [7] S.H. Cho, H.G. Choi, J.Y. Yoo, Direct numerical simulation of fluid flow laden with many particles, *Int. J. Multiphase Flow* 31 (4) (2005) 435–451.
- [8] J. Ding, D. Gidaspow, A bubbling fluidisation model using theory of granular flow, *AIChE J.* 36 (4) (1990) 523–538.
- [9] N. Dombrowski, W.R. Johns, The aerodynamic instability and disintegration of viscous liquid sheets, *J. Chem. Eng. Sci.* 18 (3) (1963) 203–214.
- [10] S. Ergun, Fluid flow through packed columns, *Chem. Eng. Prog. Symp. Ser.* 48 (2) (1952) 89–94.
- [11] R. Garg, S. Tenneti, J. Mohd-Yusof, S. Subramaniam, Direct Numerical Simulation of Gas–Solids Flow Based on the Immersed Boundary Method, in: Thomas J. O'Brien, Sreekanth Pannala, Madhava Syamlal (Eds.), *Computational Gas–Solids Flows and Reacting Systems: Theory, Methods and Practice* 2011, pp. 245–276.
- [12] D. Gidaspow, *Multiphase Flow and Fluidization: Continuum and Kinetic Theory Descriptions with Applications*, Academic Press, Boston, 1994. 315–316.
- [13] R.J. Hill, D.L. Koch, A.J.C. Ladd, The first effects of fluid inertia on flows in ordered and random arrays of spheres, *J. Fluid Mech.* 448 (2001) 213–241.
- [14] R.J. Hill, D.L. Koch, A.J.C. Ladd, Moderate-Reynolds-number flows in ordered and random arrays of spheres, *J. Fluid Mech.* 448 (2001) 243–278.
- [15] K. Hong, W. Wang, Q. Zhou, J. Wang, J. Li, An EMMS-based multi-fluid model (EFM) for heterogeneous gas–solid riser flows: part I. formulation of structure-dependent conservation equations, *J. Chem. Eng. Sci.* 75 (2012) 376–389.
- [16] H.H. Hu, N.A. Patankar, M.Y. Zhu, Direct numerical simulations of fluid–solid systems using the arbitrary Lagrangian–Eulerian technique, *J. Comput. Phys.* 169 (2) (2001) 427–462.
- [17] Y. Igci, S. Pannala, S. Benyahia, S. Sundaresan, Validation studies on filtered model equations for gas–particle flows in risers, *Ind. Eng. Chem. Res.* 51 (4) (2012) 2094–2103.
- [18] J. Israelachvili, *Intermolecular and Surface Forces*, 3rd edition Academic Press, London, UK, 1991, ISBN 978-0-12-375182-9. (ALK. paper).
- [19] J.T. Jenkins, C. Zhang, Kinetic theory for identical, frictional, nearly elastic spheres, *Phys. Fluids* 14 (2002) 1228–1235.
- [20] S. Karimipour, T. Pugsley, Application of the particle in cell approach for the simulation of bubbling fluidized beds of Geldart A particles, *J. Powder Technol.* 220 (2012) 63–69.
- [21] J. Li, W. Ge, W. Wang, N. Yang, X. Liu, L. Wang, X. He, X. Wang, J. Wang, M. Kwauk, From Multiscale Modeling to Meso-Science, A Chemical Engineering Perspective Principles, Modeling, Simulation, and Application, Springer, Heidelberg New York Dordrecht London, 2013, <http://dx.doi.org/10.1007/978-3-642-35189-1> (Library of Congress Control Number: 2012954048).
- [22] J. Li, M. Kwauk, Particle–Fluid Two Phase Flow, The Energy Minimization Multiscale Method, Metallurgy Industry Press, Beijing, 1994.
- [23] X. Liu, X. Xu, W. Zhang, Numerical simulation of dense particle gas two-phase flow using the minimal potential energy principle, *J. Univ. Sci. Technol. Beijing Miner. Metall. Mater.* 13 (4) (2006) 301–307.
- [24] B. Lu, W. Wang, J. Li, Searching for a mesh-independent sub-grid model for CFD simulation of gas–solid riser flows, *J. Chem. Eng. Sci.* 64 (15) (2009) 3437–3447.
- [25] J. Ma, W. Ge, X. Wang, J. Wang, J. Li, High-resolution simulation of gas–solid suspension using macro-scale particle methods, *J. Chem. Eng. Sci.* 61 (21) (2006) 7096–7106.
- [26] T. McKeen, T. Pugsley, Simulation and experimental validation of a freely bubbling bed of FCC catalyst, *J. Powder Technol.* 129 (1–3) (2003) 139–152.
- [27] T. Mikami, H. Kamiya, M. Horio, Numerical simulation of cohesive powder behaviour in a fluidized bed, *Chem. Eng. Sci.* 53 (10) (1998) 1927–1940.
- [28] C.C. Milioli, F.E. Milioli, W. Holloway, K. Agrawal, S. Sundaresan, Filtered two-fluid models of fluidized gas–particle flows: new constitutive relations, *AIChE J.* 59 (9) (2013) 3265–3275.
- [29] T. Nomura, T.J.R. Hughes, An arbitrary Lagrangian–Eulerian finite element method for interaction of fluid and a rigid body, *J. Comput. Methods Appl. Mech. Eng.* 95 (1) (1992) 115–138.
- [30] S. Pannala, M. Syamlal, T.J. O'Brien, *Computational Gas–Solids Flows and Reacting Systems: Theory, Methods and Practice*, Engineering Science Reference 2011. (13: 978-1615206513).
- [31] H.Y. Qi, F. Li, B. Xi, C. You, Modeling of drag with the Eulerian approach and EMMS theory for heterogeneous dense gas–solid two-phase flow, *J. Chem. Eng. Sci.* 62 (6) (2007) 1670–1681.
- [32] L. Schiller, A. Naumann, A Drag Coefficient Correlation, VDI Zeitung Publications, vol. 771935. 318–320.
- [33] J.P.K. Seville, C.D. Willett, P.C. Knight, Interparticle force in fluidization: a review, *J. Powder Technol.* 113 (3) (2000) 261–268.
- [34] N. Sharma, N. Patankar, A fast computation technique for the direct numerical simulation of rigid particulate flows, *J. Comput. Phys.* 205 (2) (2005) 439–457.
- [35] A. Samuelsberg, B.H. Hjertager, Computational modeling of gas/particle flow in a riser, *AIChE J.* 42 (6) (1996) 1536–1546.
- [36] M. Syamlal, W. Rogers, T.J. O'Brien, MFX Documentation; Theory Guide, Technical Note, U.S. Department of Energy, Office of Fossil Energy, Morgantown Energy Technology Center, Morgantown, West Virginia, 1993.
- [37] M. Syamlal, W. Rogers, T.J. O'Brien, MFX Documentation: Volume 1, Theory Guide, National Technical Information Service, Springfield, VA, 1993 (Appendix A).
- [38] M. Syamlal, T.J. O'Brien, Fluid dynamic simulation of O3 decomposition in a bubbling fluidized bed, *AIChE J.* 49 (11) (2003) 2793–2801.
- [39] S. Tenneti, R. Garg, S. Subramaniam, Drag law for monodisperse gas–solid systems using particle-resolved direct numerical simulation of flow past fixed assemblies of spheres, *Int. J. Multiphase Flow* 37 (9) (2011) 1072–1092.

- [40] S. Tenneti, S. Subramaniam, Particle-resolved direct numerical simulation for gas–solid flow model development, *Annu. Rev. Fluid Mech.* 46 (2013) 199–230.
- [41] Y. Tsuji, T. Kawaguchi, T. Tanaka, Discrete particle simulation of a fluidized bed, *Powder Technol.* 77 (1) (1993) 79–87.
- [42] J.J. Van Deemter, E.T. van der Laan, Momentum and energy balances for dispersed two-phase flow, *J. Appl. Sci. Res. Sect. A* 10 (1961) 102–108.
- [43] M.A. van der Hoef, M. van Sint Annaland, N.G. Deen, J.A.M. Kuipers, Numerical simulation of dense gas–solid fluidized beds: a multiscale modeling strategy, *Annu. Rev. Fluid Mech.* 40 (2008) 47–70.
- [44] M.A. van der Hoef, R. Beetstra, J.A.M. Kuipers, Lattice-Boltzmann simulations of low-Reynolds-number flow past mono- and bidisperse arrays of sphere: results for the permeability and drag force, *J. Fluid Mech.* 528 (2005) 233–254.
- [45] C.Y. Wen, Y.H. Yu, Mechanics of fluidization, *Chem. Eng. Prog. Symp. Ser.* 62 (1) (1966) 100–111.
- [46] J. Wang, W. Ge, J. Li, Eulerian simulation of heterogeneous gas–solid flows in CFB risers: EMMS-based sub-grid scale model with a revised cluster description, *J. Chem. Eng. Sci.* 63 (6) (2008) 1553–1571.
- [47] J. Wang, A review of Eulerian simulation of Geldart A particles in gas-fluidized beds, *J. Ind. Eng. Chem. Res.* 48 (12) (2009) 5567–5577.
- [48] W. Wang, J. Li, Simulation of gas–solid two-phase flow by a multiscale CFD approach: extension of the EMMS model to the sub-grid scale level, *J. Chem. Eng. Sci.* 62 (1–2) (2007) 208–231.
- [49] Q. Xion, B. Li, G. Zhou, X. Fang, J. Xu, J. Wang, X. He, X. Wang, L. Wang, W. Ge, J. Li, Large-scale DNS of gas–solid flows on mole-8.5, *J. Chem. Eng. Sci.* 71 (2012) 422–430.
- [50] M. Xu, F. Chen, X. Liu, W. Ge, J. Li, Discrete particle simulation of gas–solid two-phase flows with multi-scale CPU–GPU hybrid computation, *J. Chem. Eng.* 207–208 (2012) 746–757.
- [51] M. Ye, M.A. van der Hoef, J.A.M. Kuipers, From discrete particle model to a continuous model of Geldart A particles, *J. Chem. Eng. Res. Des.* 83 (7) (2005) 833–843.
- [52] M.A. Ye, M.A. van der Hoef, J.A.M. Kuipers, The effects of particle and gas properties on the fluidization, *J. Chem. Eng. Sci.* 60 (16) (2005) 4567–4580.
- [53] M.A. Ye, M.A. van der Hoef, J.A.M. Kuipers, Two-fluid modeling of Geldart A particles in gas-fluidized beds, *J. Particuology* 6 (6) (2008) 540–548.
- [54] X. Yin, S. Sundaresan, Drag law for bidisperse gas–solid suspensions containing equally sized spheres, *J. Ind. Eng. Chem. Res.* 48 (1) (2009) 227–241.
- [55] N. Yang, W. Wang, W. Ge, J. Li, CFD simulation of concurrent-up gas–solid flow in circulating fluidized beds with structure-dependent drag coefficient, *J. Chem. Eng.* 96 (1–3) (2003) 71–80.
- [56] D.Z. Zhang, W.B. Vanderheyden, The effects of mesoscopic structures on the macroscopic momentum equations for two-phase flows, *Int. J. Multiphase Flow* 28 (5) (2002) 805–822.
- [57] L.M. Zou, Y.C. Guo, C.K. Chan, Cluster-based drag coefficient model for simulating gas–solid flow in a fast-fluidized bed, *J. Chem. Eng. Sci.* 63 (4) (2008) 1052–1061.
- [58] K. Agrawal, P.N. Loezos, M. Syamlal, S. Sundaresan, The role of meso-scale structures in rapid Gas-solid flows, *J. Fluid Mech* 445 (2001) 151–185.
- [59] C.K.K. Lun, S.B. Savage, D.J. Jeffrey, N. Chepuriniy, Kinetic theories for granular flow: inelastic particles in Couette flow and slightly inelastic particles in a general flowfield, *J. Fluid Mech.* 140 (1984) 223–256.
- [60] B. Chu, *Molecular Forces*, Wiley, New York, 1967.